Proceedings of the ASME 2010 3rd Joint US-European Fluids Engineering Summer Meeting and 8th International Conference on Nanochannels, Microchannels, and Minichannels
FEDSM-ICNMM2010
August 1-5, 2010, Montreal, Canada

FEDSM-ICNMM2010-30811

TURBULENT WAKE OF SURFACE-MOUNTED FINITE ASPECT RATIO BLUFF BODIES: EFFECT OF ASPECT RATIO AND CROSS SECTION SHAPE

Pooria Sattari*
Department of Mechanical and Manufacturing Engineering,
University of Calgary
Calgary, Alberta, Canada
Email: psattari@ucalgary.ca

Jason A. Bourgeois
Department of Mechanical and Manufacturing Engineering,
University of Calgary
Calgary, Alberta, Canada

Robert J. Martinuzzi
Department of Mechanical and Manufacturing Engineering,
University of Calgary
Calgary, Alberta, Canada

ABSTRACT

Dynamic shedding characteristics in the wake of vertical, surface mounted square and circular cylinders of aspect ratio (H/D) 0.5, 2, 4 and 8 are investigated using high frame-rate particle image velocimetry and thermal anemometry for Reynolds numbers, based on the obstacle width/diameter ranging between 6×10^3 and 10^5. The wavelet transform was used to determine the instantaneous phase relationship for either pressure or velocity fluctuations on opposite sides of the obstacles. Except for the smallest aspect ratio, two shedding modes with different vortex configurations are observed in the formation region: i) Alternate formation of vortices accompanied by high-amplitude fluctuation; ii) Events of simultaneous formation of two vortices resulting in low-amplitude activity and varying phase relationship between opposing sides. These counter-rotating coexisting vortices are generally shed alternately. In the case of aspect ratio 0.5 prism, periodic activity is irregular and the shedding behavior is different from higher aspect ratio bodies.

NOMENCLATURE

D	Obstacle width/diameter
f	Frequency
H	Obstacle height
Im	Imaginary part
p	Instantaneous pressure
R	Real part
Re	Reynolds number
St	Strouhal number $(f D/U_\infty)$
t	Time
t^*	Non-dimensional time
u	Instantaneous streamwise velocity
u'	Fluctuation velocity (=u –U)
u_{rms}	Root mean square of streamwise velocity
U	Mean streamwise velocity
U_∞	Free stream velocity
W	Complex wavelet transform
x	Streamwise coordinate
y	Cross-stream (span-wise) coordinate
z	Vertical coordinate
δ	Boundary layer thickness
θ	Phase angle
λ	Wavelet scale
τ	Wavelet time lag
ϕ	Phase angle
Φ	Power spectral density
ψ	Wavelet function

INTRODUCTION

Periodic vortex shedding in the turbulent wake of surface mounted finite aspect ratio bluff bodies is a complex three-dimensional phenomenon which involves the interaction of non-steady vortical structures of different scales, orientations and intensities. The three main coherent structures associated with the flow around these bodies include the horseshoe vortices generated by the negative pressure gradient upstream of the obstacle at the wall-body junction, the Karman-like shed

* Address all correspondence to this author.

structures in the mid-span, and the tip vortices. One expects the contribution of each of these structures to the overall flow field to vary with obstacle shape and aspect ratio (AR=*H/D*). Yet, there are few comprehensive comparative parametric studies.

The behavior of the wake velocity and obstacle surface pressure is characterized by nearly constant frequency oscillations with intervals of high-amplitude fluctuations interspersed with low-amplitude activity of varying length depending on the aspect ratio and cross-sectional shape. Generally, the phase relationship between fluctuations on opposing sides of the wake may vary along the height and the distance downstream of the obstacle.

Mainly based on visualizations at low Reynolds numbers, it has been observed [1-2] that below a critical aspect ratio (varying between 1 and 7 depending on boundary layer characteristics and obstacle geometry [3]) the shedding regime changes from anti-symmetric (Karman type) to symmetric (arch type). It was also suggested that for higher aspect ratio circular cylinders, towards the free end, the shedding becomes symmetric [2].

Wang and Zhou [4] and Wang et. al. [5] used a Q-criterion method to detect vortex cores in the flow field based on low-frame rate (15 fps) PIV measurements in planes parallel to the free end along body's height. They found that as the free end is approached, the probability of symmetric arrangements of shed vortices increased relative to anti-symmetric arrangements in the wake for aspect ratio 5 and 7 prisms at Reynolds numbers ~10000.

The observed symmetry has been attributed to the suppression of the Karman-type shedding process due to the downwash generated by tip vortices near the free end. However, the formation mechanism of these tip vortices and how these interact with the formation region in the obstacle lee are still not well understood [4, 6-8]. Whether the same mechanism exists for both circular and square sections and whether the formation of the tip vortices is inherently periodic or modulated by the downstream shedding remains unclear.

In the present work we aim to investigate in greater detail the dynamic shedding behavior for square and circular cylinders of aspect ratios 0.5, 2, 4 and 8. High frame-rate particle imaging velocimetry (HFPIV) and thermal anemometry were used as experimental tools. A complex wavelet transform technique was implemented for the instantaneous determination of the shedding phase from opposite sides of these obstacles along their height. Surface shear stress field patterns deduced from oil film visualizations were used to examine the effect of wake dynamics on the mean flow pattern.

EXPERIMENTAL SETUP

The experiments were carried out in an open-section wind tunnel at the University of Calgary with a 0.5m diameter circular working section. Seven turbulence-reduction mesh screens are installed upstream of the contraction channel (area contraction ratio 16:1) resulting in a free stream turbulence intensity below 0.5% at the free-stream velocity used for the experiments ($U_\infty \approx 15$ m/s).

Circular and square section cylinders with aspect ratios 0.5, 2, 4 and 8 were machined from aluminum. The height of all the obstacles was 50.8mm. Reynolds numbers based on obstacle width, D and free stream velocity, U_∞ ranged between 6×10^3 and 10^5. Pressure taps with 0.35mm diameter were drilled 12.7mm (z/H=0.25) from the base on both side faces of AR=4 prism for pressure measurements. The obstacle and coordinate system nomenclature are summarized in Figure 1.

A flat plate machined from aluminum with a sharp leading edge was used to generate the boundary layer flow. All obstacles were mounted 0.2m from the plate leading edge where the boundary layer thickness was approximately 8mm (δ/H=0.16). The boundary layer mean and rms (root mean square) streamwise profiles at this location (with the obstacle removed) are presented in Figure 2.

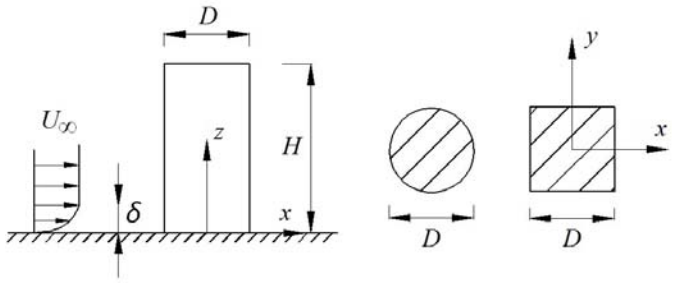

FIGURE 1. SCHEMATIC OF THE OBSTACLE AND COORDINATE SYSTEM NOMENCLATURE.

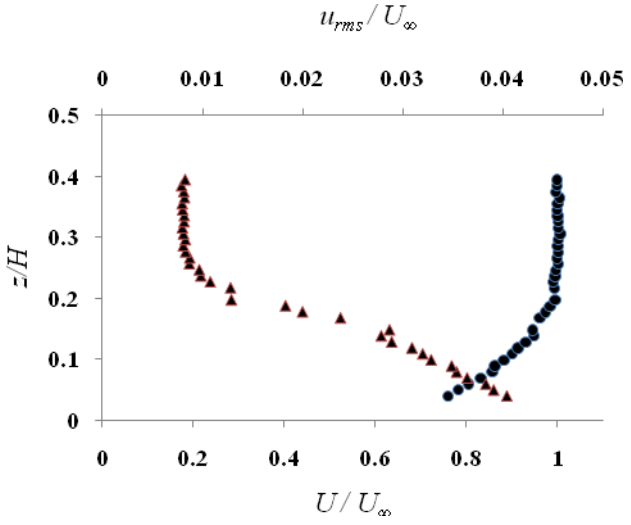

FIGURE 2. BOUNDARY LAYER -●-MEAN (U/U_∞) -▲-RMS (u_{rms}/U_∞) PROFILES AT THE OBSTACLE LOCATION (OBSTACLE REMOVED)

A LaVision high frame rate particle image velocimetery (PIV) system was used for planar velocity field measurements. The laser sheet illumination was generated by a high power 527nm Nd-Yag pulsed laser. A HighSpeedStar 5 camera (1024×1024 pixels) was used to capture images in the double frame mode (dt=50μs) at a 1000 fps sampling rate. The camera field of view was approximately 195mm×195mm. A 32 × 32 pixel interrogation window (6mm×6mm) with 50% overlap in both directions resulting in a vector separation of 3mm was used. Two Laskin particle generators placed outside (upstream) of the tunnel were used to generate seeding olive oil particles (mean diameter of approximately 1μm).

Differential pressure transducers (All Sensors Corp, model 1 INCH-D1-4V-MINI) were used to measure pressure fluctuations simultaneously on both sides of the aspect ratio 4 prism. The pressure transducer and PIV data acquisition were synchronized through TTL trigger signals. The differential pressure transducers had a range of 0-250 Pa and a resolution of 0.26 Pa. The pressure transducers were calibrated against an inclined manometer using a known pressure source. The pressure sensing system dynamic response was estimated against a flush-mounted transducer. Pressure data was sampled at 10240Hz for 10s.

For velocity measurements and spectral analysis, single hotwire anemometers (probe model TSI 1210-20, bridge model TSI IFA-100) operated in constant-temperature mode were used. Two wires were placed at either y/D=±1.2 or y/D=±2. A three-axis motorized computer-controlled traverse unit was used to position the wires at streamwise locations x/D=0.5, 1, 2 and 4 along desired heights. One additional wire measured the free stream velocity. Hotwires were calibrated against a Pitot tube. Data was sampled simultaneously with pressure data at 10240Hz for a record length of 100,000 samples.

A 24-bit National Instruments (NI-9227) data acquisition system with built-in anti-aliasing filter and LabView program were used to record hotwire and pressure data.

A mixture of oil, kerosene and graphite was used for the oil film visualizations to obtain the mean surface flow patterns. The tunnel was operated after the mixture had been applied and until the mixture dried.

WAVELET TRANSFORM METHOD

To investigate the phase angle of vortex shedding in the wake of the obstacles, the instantaneous velocities at y/D=±1.2 and y/D=±2 were measured simultaneously using two hotwire probes. Complex wavelet transforms were used to extract the instantaneous shedding phase difference between two signals [9]. The complex wavelet transform of a velocity signal $u(t)$ with a scale λ (proportional to the inverse of frequency) and time lag τ is defined as

$$W(\lambda,\tau)=\int_{-\infty}^{\infty}u(t)\psi^{*}{}_{\lambda,\tau}(t)dt \qquad (1)$$

where the asterisk denotes the complex conjugate, and the wavelet function for a given scale and time lag is

$$\psi_{\lambda,\tau}(t)=\frac{1}{\sqrt{\lambda}}\psi\left(\frac{t-\tau}{\lambda}\right) \qquad (2)$$

The analyzing wavelet used is the complex Morlet wavelet. It is constructed from a harmonic oscillation with an amplitude that has a Gaussian envelope. The Morlet wavelet with bandwidth, f_b, and center frequency, f_c, is defined as

$$\psi(t)=\frac{1}{\sqrt{\pi f_b}}e^{i\,2\pi f_c t}e^{-t^2/f_b} \qquad (3)$$

The phase of the vortex shedding cycle is determined by $\phi=\tan^{-1}\mathrm{Im}(W)/R(W)$ where W is the complex value of the wavelet transform at the scale associated with the frequency of vortex shedding as taken from the peak of the Fourier power spectra. The mother wavelet (which is the basic wavelet which is subsequently scaled and shifted in time) used had $f_b=1.5$Hz and $f_c=1$Hz and is shown in Figure 3. The Mother wavelet is then scaled to have a center frequency equal to the frequency peak in the Fourier power spectra and the convolution integral (1) is taken.

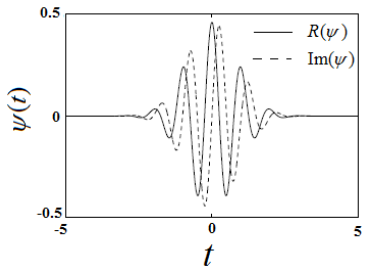

FIGURE 3. COMPLEX MORLET USED FOR ANALYSIS

RESULTS AND DISCUSSIONS

In this section synchronized PIV/pressure measurements are presented for the geometry AR=4 square cylinder in order to investigate the nature of vortex formation in the base region and the shedding of the vortices. All presented PIV measurements are from a horizontal plane at z/H=0.5.

Approximately 8 PIV images per shedding cycle were captured enabling to track the evolution of vortices (shedding frequency was $f_s=122$ Hz corresponding to St=0.10). By inspecting the PIV snapshots for different shedding cycles, two typical vortex configurations at the lee of the obstacle are distinguished. One configuration corresponds to shedding periods during which vortices of opposite sign circulation are formed and shed alternatively in a fashion similar to the classical two-dimensional Karman process. A typical sequence of such a configuration is illustrated in Figure 4 using sectional streamlines in the stationary frame of reference. These

snapshots are separated by one quarter of the nominal shedding period ($\Delta t^* = \Delta t \times f_s = 0.25, \Delta t$: PIV sampling interval).

In the second configuration, two counter-rotating vortices exist simultaneously in the base region throughout the shedding cycle as shown in Figure 5.

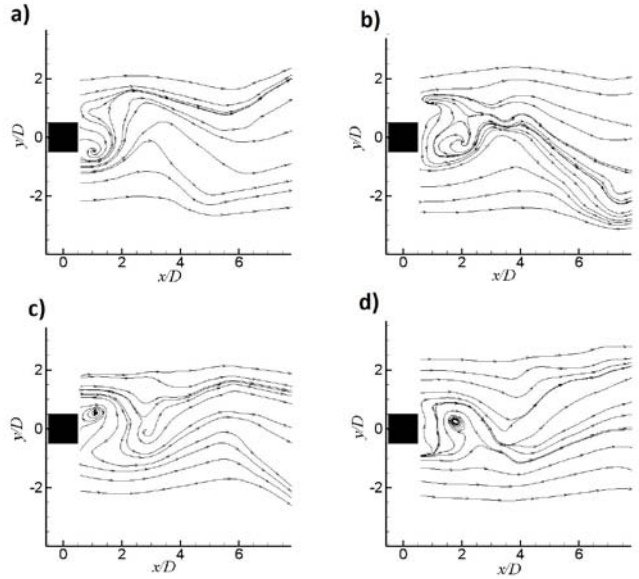

FIGURE 4. SECTIONAL STREAMLIENS FROM PIV SNAPSHOTS (*z/H*=0.5) REPRESENTING ALTERNATE FORMATION OF VORTICES IN THE BASE REGION (SNAPSHOTS SEPARATED BY $\Delta t = 0.002\ s$, $\Delta t^* = 0.25$)

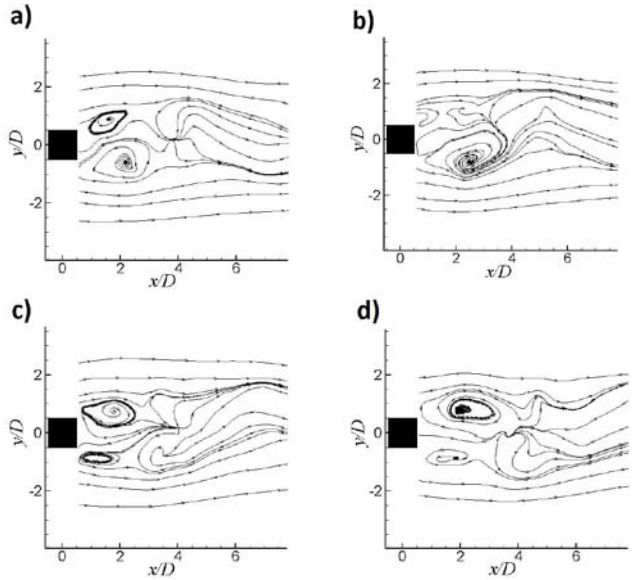

FIGURE 5. SECTIONAL STREAMLIENS FROM PIV SNAPSHOTS (*z/H*=0.5) REPRESENTING COEXISTENCE OF TWO VORTICES IN THE BASE REGION (SNAPSHOTS SEPARATED BY $\Delta t = 0.002\ s$, $\Delta t^* = 0.25$)

Pressure traces on both side faces of the obstacle (relative to free stream static pressure) corresponding to the PIV snapshots in Figures 4 and 5 (PIV and pressure measurements were synchronized) are presented in Figure 6a. It is noted that the first vortex formation mode (i.e. alternate formation) is accompanied by high-amplitude well-organized fluctuations. In contrast, during the time intervals when two counter-rotating vortices coexist in the formation region, the pressure fluctuations on the obstacle side faces have much lower amplitude.

Figure 6b illustrates the phase relationship between pressure fluctuations on opposite sides for the same time interval. During high-amplitude intervals, the phase difference is nearly constant (180° out-of-phase), whereas during low-amplitude intervals, the phase relationship is less regular and changes significantly. A similar behavior is observed in the velocity time series measured close to obstacle in the vicinity of the formation region (*x/D*<2).

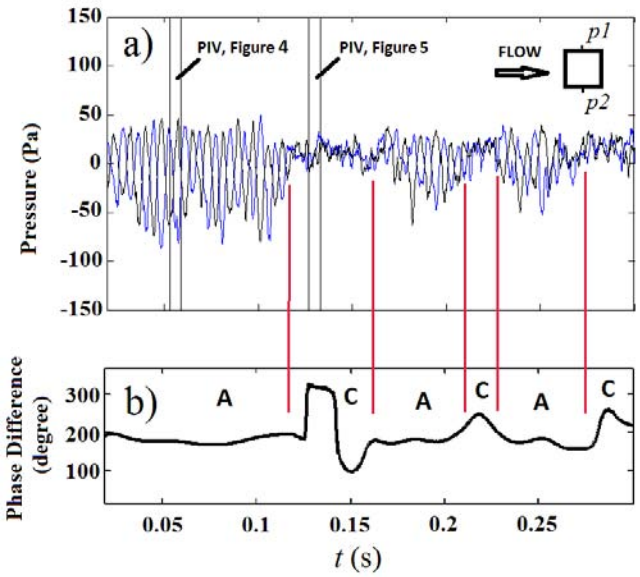

FIGURE 6. a) PRESSURE FROM OBSTACLE'S OPPOSING SIDES SYNCHRONIZED WITH PIV SNAPSHOTS IN FIGURES 4 AND 5, b) CORRESPONDING PHASE DIFFERENCE. –A-: ALTERNATE VORTEX FORMATION, -C-: COEXISTENCE OF TWO BASE VORTICES

Figure 7 shows a sample of simultaneously recorded side face pressures and downstream velocities (*x/D*=4, *y/D*=±2, *z/H*=0.5). As expected, during high-amplitude intervals, both pressure and downstream velocity fluctuations on opposing sides are both ~180° out-of-phase. During the low-amplitude intervals (observed in the pressure signals), however, the behavior observed in the formation region differs from that observed downstream. Whereas the phase relationship between the pressure fluctuation on opposing faces varies significantly and is often in-phase, the amplitude of the downstream velocity fluctuations is less modulated, the periodicity more easily

recognized and the fluctuations on opposing sides are again out-of-phase (~180°).

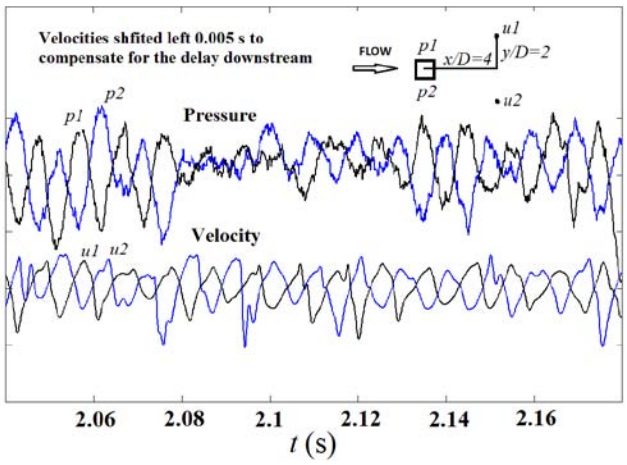

FIGURE 7. SIMULATANEOUS VELOCITY AND PRESSURES FOR AR=4 PRISM . VELOCITIES MEASURED AT *x/D*=4, *y/D*=2, *z/H*=0.5, (*p1&p2*, *u1&u2*: PRESSURES AND VELOCITIES ON OPPOSING SIDES, RESPECTIVELY)

Closer inspection of the shedding sequence during the low-amplitude intervals suggests that, at a given instant during the shedding cycle, only a portion of the circulation from one of the coexisting vortices is shed (cf. Figure 5b). Generally, this partial shedding process occurs alternately from opposing base vortices. However, the time interval between the shedding of opposite circulation vortices varies randomly from cycle-to-cycle. As a result, the spacing between vortex pairs immediately downstream of the formation region, varies greatly, giving rise to large variations in the phase differences as observed in Figure 6b (intervals marked C). Nevertheless, as will be shown later, the probability of in-phase shedding remains small. Since only a portion of the circulation in the base region is transferred to the shed vortices, these are weaker than those observed during the alternating events of the first configuration, which may account for the lower fluctuation amplitudes.

Effect of Aspect Ratio and Cross Section Shape

This section focuses on the differences observed in the wake dynamics between square and circular section cylinders at different aspect ratios.

Sample time series of the fluctuation velocity, u', for the square section cylinders of AR=2, 4 and 8 for two elevations are shown in Figure 8. For AR=4 and AR=8 prisms, as the free end is approached the modulation in the signal becomes stronger and low-amplitude activity is more pronounced. This observation is consistent with observations made previously [2, 4]. These weak fluctuations in the free-end region occur much more frequently for AR=8 compared to AR=4. In the case of AR=2, however, no noticeable differences in the fluctuation amplitude are observed between the free end and wall-junction regions. Hence, for this case, the influence of the tip flow appears to extend over the entire height of the obstacle. Unexpectedly, perhaps, the low-amplitude activity occurs less frequently than higher aspect ratio obstacles. For AR = 0.5, the amplitude is randomly modulated and the shedding activity differs significantly from that observed for higher aspect ratio obstacles.

Figure 9 illustrates the probability density function (PDF) of instantaneous phase differences at *x/D* =1, *y/D*=±1.2 for prisms of different aspect ratios. The peak in all of the PDFs occurs in the proximity of 180°. The PDF distribution, except for AR = 0.5, shows that in-phase events are very rare. These observations confirm the domination of out-of-phase shedding behavior observed in PIV snapshots, and velocity and pressure time series. At *z/H*=0.8 the PDF is broader for AR=4 and 8 obstacles due to the more pronounced low-amplitude activity in that region whereby the variations in the instantaneous phase manifest themselves in a broader PDF. Nevertheless, in-phase events remain rare. Thus even during the low-amplitude intervals, vortices are shed mostly in an alternating fashion even though two counter-rotating vortices exist in the base region. For AR = 2 the PDFs are very similar to those observed for larger aspect ratio obstacles near the free end. For AR=0.5, the PDF is much broader than the other cases. For this case, probability of in-phase behavior is non-negligible, suggesting a distinct shedding pattern, different from higher aspect ratio geometries.

The standard deviation of the relative phase may be used as a measure to quantify the broadness of the PDF. An increase in the standard deviation may be associated with an increase in the low-amplitude fluctuations (mode with coexisting base vortices). The standard deviations for both circular and square section cylinders are presented in Figure 10 at two streamwise locations (*x/D*=1 and *x/D*=4). For large aspect ratio square cylinders, around the formation region (*x/D*=1), the standard deviation increases with height, consistent with the PDF trends observed in Figure 9. Downstream (*x/D*=4), the standard deviation increases less with height suggesting a rearrangement of the vortices shed during the low-amplitude intervals as described in relation to Figure 5. The reduction in the standard deviation (as a measure of the broadness of the PDF) is consistent with the increase in "out-of-phase" behavior observed downstream as shown in Figure 7.

For AR=2, however, the standard deviation does not change with height or downstream location, but is at levels comparable to those found near the free end for larger aspect ratios, again suggesting that the influence of the tip flow extends over the entire height. For the AR=0.5 square cylinder, the standard deviation (not shown for brevity) is of the order of 100° and does not change with location.

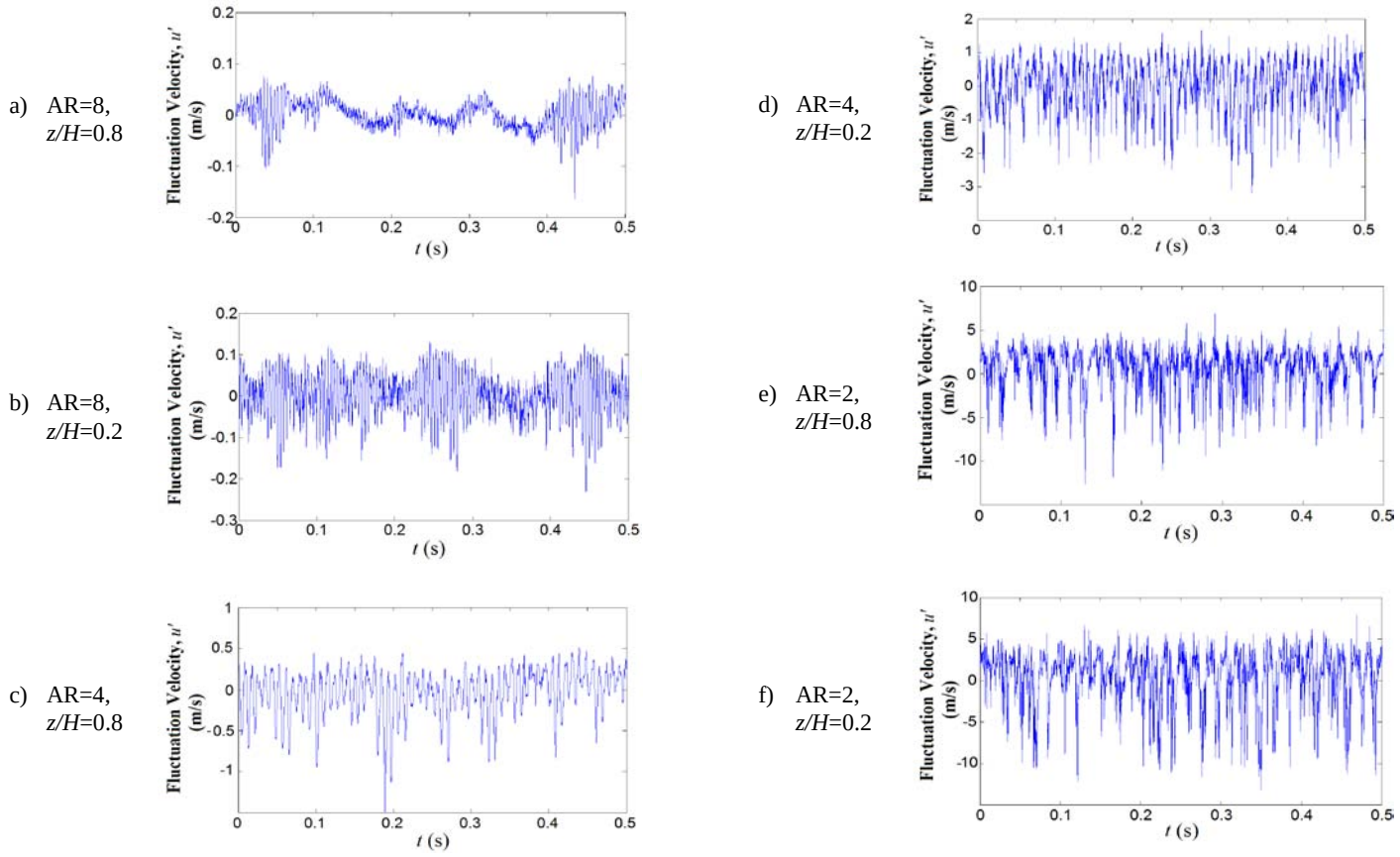

FIGURE 8. VELOCITY TIME SERIES FOR AR=8, 4 AND 2 SQUARE CYLINDERS MEASURED AT *x/D*=1, *y/D*=1.2

For the circular cylinders, the interpretation of the results obtained is less clear. Considering points for $z/H > 0.4$, the trends in the standard deviation along the height and in the streamwise direction are similar to those observed for the square cylinder. The standard deviation for circular cylinders is higher than for square geometries, probably, due to the randomness associated with the motion of the separation line on the obstacle faces. Note that the shedding was very weak at *x/D*=1 for AR=8 and therefore no reliable wavelet analysis could be made. Near the wall-obstacle junction (at $x/D = 1$), however, the standard deviation for the circular cylinder is much larger than above. This effect is not observed at *x/D*=4 or for the square geometry. This effect may be related to the nature of the location of the flow separation line on the obstacle face. Near the junction, the presence of the horseshoe vortex induces pressure gradients along the faces which may interfere with both the location of the separation line and the circulation flux generated at the separation point. As the obstacle aspect ratio is further reduced to one (or less), periodicity is no longer observed for the circular geometry. For the square geometry, the location of flow separation is fixed by the sharp edge and thus less sensitivity to the horseshoe vortex would be expected. While similar explanations to account for the differences between rectangular and circular cylinder geometries have been offered before [1-3], it is noted that this disruption of the junction region formation process has consequences on the downstream flow and vortex topology which still have not been satisfactorily resolved.

Figure 11 illustrates power spectra at different heights for square and circular cylinders. For the square cylinder geometries, the spectra for AR=2, 4 and 8 show strong, distinctive peaks with little loss of power as the tip is approached. For AR=0.5, the spectra are broad with accumulations of energy about the nominal shedding frequency. This weak periodicity is confirmed from the velocity correlation functions shown in Figure 12a for AR=0.5 at *x/D*=1, *y/D*=±1.2, *z/H*=0.8. The cross-correlation function shows that the mean phase difference is close to 180°, as indicated in Figure 9d, but true in-phase events occur with higher probability than for other obstacles as suggested by the time series in Figure 12b and the PDF of Figure 9d.

a) AR=8

b) AR=4

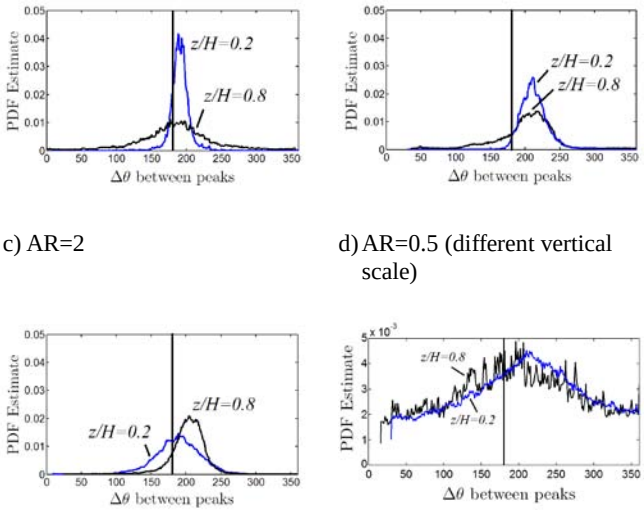

c) AR=2

d) AR=0.5 (different vertical scale)

FIGURE 9. PDFS FOR SQUARE SECTION CYLINDERS EXTRACTED FROM WAVELET ANALYSIS BASED ON VELOCITY MEASUREMENTS AT *x/D*=1, *y/D*=±1.2 (SOLID LINE SHOWS 180 DEGREES PHASE DIFFERENCE)

Square cylinder

Circular cylinder

a) AR=8

b) AR=8

c) AR=4

d) AR=4

e) AR=2

f) AR=2

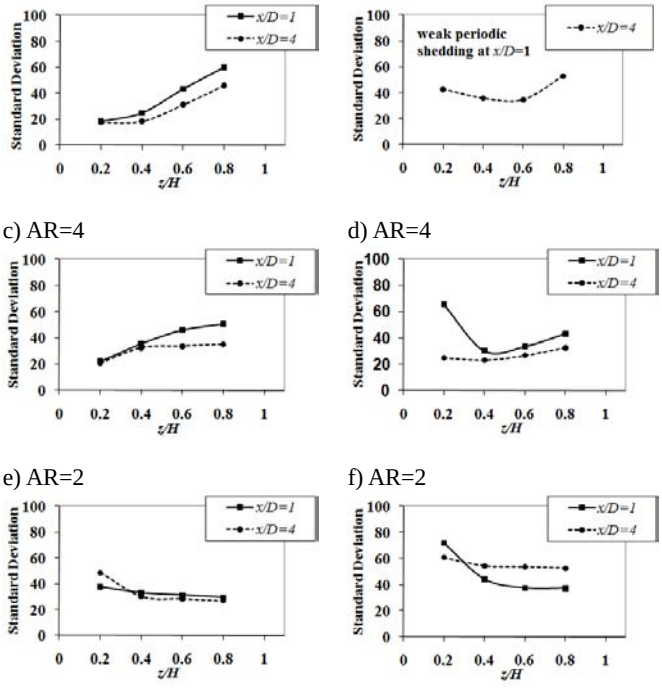

FIGURE 10. STANDARD DEVIATION OF PDF FOR SQUARE AND CIRCULAR CYLINDERS AT *x/D*=1 AND 4, *y/D*=±1.2

For circular cylinders, also shown in Figure 11, the spectral peaks are generally broader, probably due to the non-fixed nature of the separation region. An important difference to the behavior noted for the square cylinders is a loss of power near the free end and in the wall junction region. The latter observation can be related to the interference with the horseshoe vortex as stated previously. However, the loss of fluctuation energy near the free end suggests that the nature of the tip flow may also change. Differences in the strength of vortices at the tip of circular cylinders have been reported [7-8], but there seems to be a lack of consensus in reported results. For example down and upwash (i.e. difference in sense of rotation) have both been reported. These differences may be related to the effect of the boundary layer thickness.

Square cylinder

Circular cylinder

a) AR=8

b) AR=8

c) AR=2

d) AR=2

e) AR=0.5 (scale of horizontal axis changed for clarification)

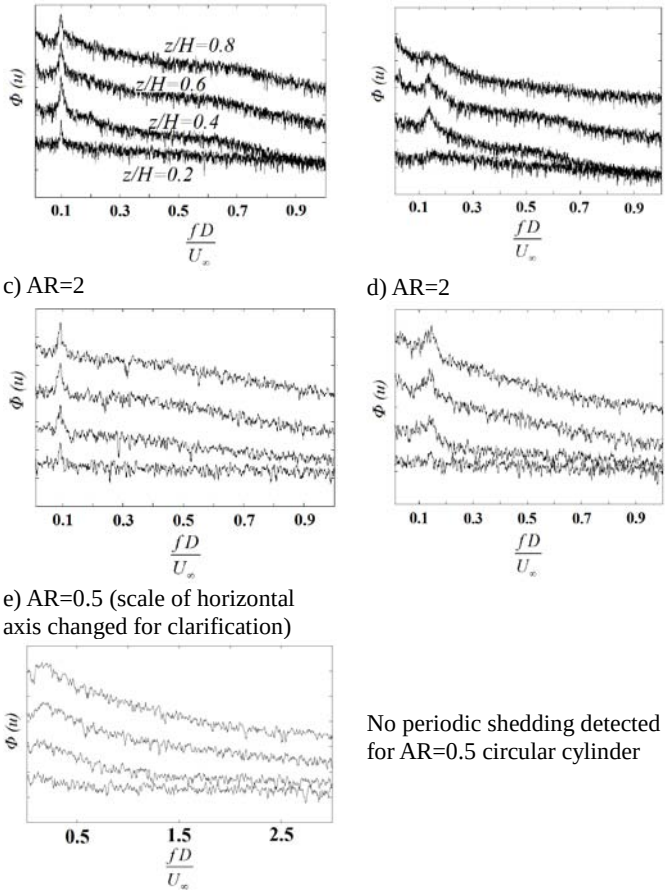

No periodic shedding detected for AR=0.5 circular cylinder

FIGURE 11. POWER SPECTRA FOR SQUARE AND CIRCULAR CYLINDERS AT *z/H*=0.2, 0.4, 0.6 AND 0.8, *x/D*=1, *y/D*=1.2. (GRAPHS SHIFTED VERTICALLY FOR CLARIFICATION)

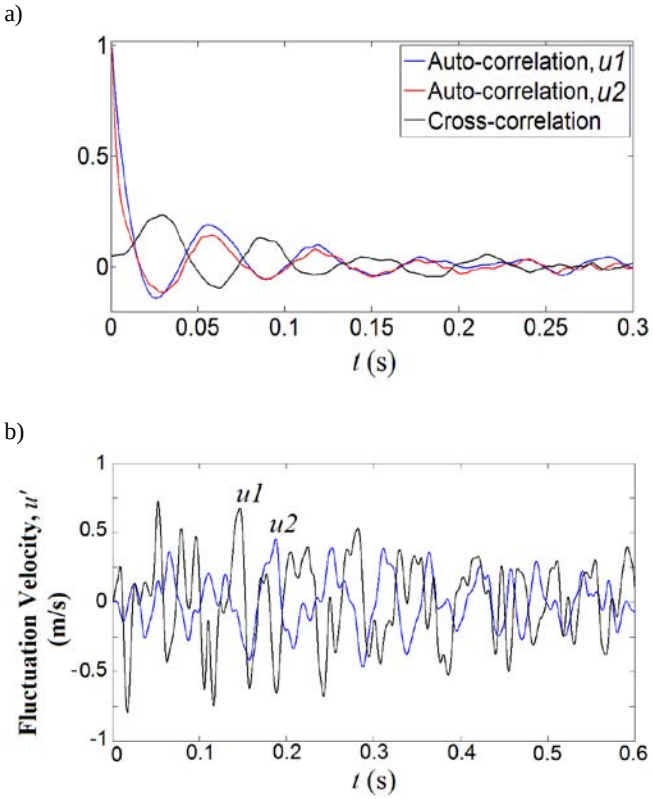

FIGURE 12. a) VELOCITY CORRELATIONS ON OPPOSING SIDES, b) VELOCITY TIME SERIES ON OPPOSING SIDES OF AR=0.5 PRISM AT *x/D*=1, *y/D*=±1.2, *z/H*=0.8

In order to examine the influence of aspect ratio on the mean flow field, oil film visualizations were carried out. Oil film visualization is a useful tool in identifying the footprint of large scale structures in the flow field. Representative images for two aspect ratios are shown in Figure 13 for the square and circular geometry. Clearly, a deeper penetration of the flow into the wake is distinguished for AR=4 by considering the stronger necking in the wake. Furthermore, the circulation zones and saddle points become closer and are merged together in the case of AR=4 compared to AR=2 obstacles. It is noted that the surface stress lines associated with the horseshoe vortex tend to be closer to the circular than the square obstacle, which is consistent with the observation that the streamwise structure is more likely to interfere with the vortex formation region in the junction region. These differences show a significant change in the mean flow pattern topology and indicate that important differences in the vortex structure in the wake exist for these two geometries.

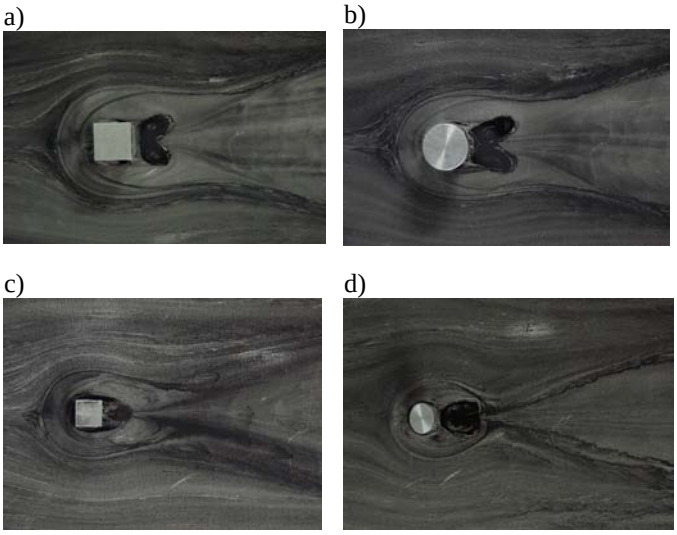

FIGURE 13. OIL FILM VISUALIZATIONS (TOP VIEW) a)AR=2 SQUARE, b)AR=2 CIRCULAR, c)AR=4 SQUARE, d)AR=4 CIRCULAR

Further comparison of the results obtained for the square and circular geometries is complicated by the nature of the separation line on the obstacle faces, which is critical in determining the rate at which vorticity is generated on the surface and ultimately affects the relative strength (circulation) of vortices formed and interacting in the wake. For the square cylinder, the separation is fixed at the sharp leading edges and the influence of the Reynolds number and upstream boundary layer transition is minimal over the range considered in this study. For the circular cylinder, however, the location and curvature of the separation line depends strongly on both the Reynolds number and the nature of the on-coming boundary layer. The spectra in Figure 11 suggest that the strength of the shed vortices are weaker for the circular than the square cylinder wake. Since the vorticity flux from the boundary layer, for example, is similar in both cases, the disruption of the shedding mechanism near the wall-obstacle junction is expected to be stronger for the circular than the square cylinder, as supported from Figure 10.

CONCLUSIONS

The dynamics of vortex formation and vortex shedding in the wake of AR=0.5, 2, 4 and 8 square and circular cylinders was investigated. Using synchronized pressure/PIV and thermal anemometry measurements, two competing vortex formation modes in the formation region were distinguished: (i) A mode similar to the classical shedding behind two-dimensional cylinders, i.e. alternate vortex formation on opposing sides accompanied by high-amplitude, out-of-phase pressure and velocity fluctuations; (ii) A second mode characterized by the coexistence of a pair of counter-rotating

vortices in the formation region accompanied by low-amplitude fluctuations in the wake with varying phase. These latter types of structures tend to shed anti-symmetrically as they are convected downstream. The low-amplitude events are observed more frequently as the free end is approached.

Generally the same behavior is observed for both circular and square cylinders, although the shedding behind circular cylinders is less regular due to the non-fixed nature of the separation line on the obstacle face. However, it is observed that the shedding process is different near the junction and free end region for circular cylinders when compared to square geometries. At the junction, the formation process is disrupted, which can be surmised to occur due to interference of the horseshoe vortex with the surface separation process. The square geometry appears to be less sensitive due to the sharp edges (fixed separation line) and the observation that the horseshoe structure appears further away from the obstacle. However, the differences observed at the obstacle tip are more difficult to explain and require further investigation. Results of the oil film visualizations suggest that differences in the vortex shedding dynamics are accompanied by noticeable changes in the mean wake structure, which is expected on topological grounds.

ACKNOWLEDGMENTS

The authors would like to acknowledge Natural Sciences and Engineering Research Council of Canada and Alberta Innovates Technology Futures for their financial support of this work.

REFERENCES

[1] Sakamoto, H., and Arie, M., 1983, "Vortex Shedding from a Rectangular Prism and a Circular Cylinder Placed Vertically in a Turbulent Boundary Layer", J. Fluid Mech., **126**, pp. 147-165.

[2] Okamoto, S., and Sunabashiri, Y., 1992, "Vortex Shedding From a Circular Cylinder of Finite Length Placed on a Ground Plane", J. Fluids Eng., **114**, pp. 512-521.

[3] Sumner, D., Heseltine, J. L., and Dansereau, O. J. P., 2004, "Wake Structure of a Finite Circular Cylinder of Small Aspect Ratio", Exp. Fluids, **37**, pp. 720-730.

[4] Wang, H. F., and Zhou, Y., 2009, "The Finite-length Square Cylinder near Wake", J. Fluid Mech., **638**, pp. 453-490.

[5] Wang, H. F., Zhou, Y., Chan, C. K., and Lam, K. S., 2006, "Effect of Initial Conditions on Interaction Between a Boundary Layer and a Wall-mounted Finite-length-cylinder Wake", Phys. Fluids, **18**, pp. 065106-1.

[6] Etzold, F., and Fiedler, H., 1976, "The Near-wake Structure of a Cantilevered Cylinder in a Cross-Flow", Z. Flugwiss., **24**, pp. 77-82.

[7] Roh, S. C., and Park, S. O., 2003, "Vortical Flow over the Free End Surface of a Finite Circular Cylinder Mounted on a Flat Plate", Exp. Fluids, **34**, pp. 63-67.

[8] Park, C. W., and Lee, S. J., 2000, "Free End Effects on the Near Wake Flow Structure behind a Finite Circular Cylinder", J. Wind Eng. Ind. Aerodyn., **88**, pp. 231-246.

[9] Addison, P. S., 2002, *The Illustrated Wavelet Transform Handbook: Introductory Theory and Applications in Science, Engineering, Medicine and Finance*, Taylor & Francis